PSFC/JA-10-7

Comparison of neoclassical predictions with measured flows and evaluation of a poloidal impurity density asymmetry

Marr, K.M., Lipschultz, B., Catto, P.J., McDermott R.M.*,
Reinke, M.L., Simakov, A.N.**

* ASDEX Upgrade, Garching, Germany
** Los Alamos National Lab., Los Alamos, NM

April 2010

Plasma Science and Fusion Center
Massachusetts Institute of Technology
Cambridge MA 02139 USA

This work was supported by the U.S. Department of Energy, Grant No. DE-FC02-99ER54512.

Comparison of neoclassical predictions with measured flows and evaluation of a poloidal impurity density asymmetry

K D Marr[1], B Lipschultz[1], P J Catto[1], R M McDermott[2], M L Reinke[1], A N Simakov[3]

[1]MIT Plasma Science and Fusion Center, Cambridge, MA 02139
[2]Max-Planck-Institut für Plasmaphysik, EURATOM-Association, Garching, Germany
[3]Los Alamos National Laboratory, Theoretical Division, Los Alamos, NM 87545

E-mail: kmarr@mit.edu

Abstract. The study and prediction of velocities in the pedestal region of Alcator C-Mod are important for understanding plasma confinement and transport. In this study we examine the simplified neoclassical predictions for impurity flows using equations developed for plasmas with background ions in the Pfirsch-Schlüter (high collisionality) and banana (low collisionality) regimes. B^{5+} flow profiles for H-mode plasmas are acquired using the charge-exchange recombination spectroscopy diagnostic on Alcator C-Mod and are compared with calculated profiles for the region just inside the last closed flux surface. Reasonable agreement is found between the predictions from the Pfirsch-Schlüter regime formalism and the measured poloidal velocities for the steep gradient region of the H-mode pedestals regardless of the collisionality of the plasma. The agreement is poorer between the neoclassical predictions and measured velocity profiles using the banana regime formalism. Additionally, comparisons of measured velocities from the low- and high-field sides of the plasma lead us to infer the strong possibility of a poloidal asymmetry in the B^{5+} density. This asymmetry can be a factor of 2–3 for the region of the steepest gradients, with the density at the high-field side being larger. The magnitude of the density asymmetry is found to be correlated with the magnitude of the poloidal velocity at the low-field side of the plasma.

1. Introduction

Edge velocities, both poloidal and toroidal, have been the subject of study in the last several years due to the correlation between increased flow shear, radial electric field, and improved confinement [1, 2, 3, 4]. The transition from L-mode to H-mode is marked by a sharp increase in the impurity poloidal velocity in the edge pedestal region; a characteristic that has been measured on several different tokamaks [2, 5, 6, 7]. Unfortunately, the effect of edge flows and radial electric field shear on transport is not fully understood. A clearer understanding of the mechanisms driving the flows

could provide fusion devices with the ability to control these flows and further improve confinement.

Based on the importance of pedestal velocities, much work has been done to formulate and validate a predictive theory incorporating the ion pressure and temperature profiles (for both bulk and impurity ions) as the driving force for flows on the flux surfaces [8, 9, 10]. Simplified numerical and analytical models of neoclassical particle flow have been developed to various orders for a variety of conditions, such as for heavy impurities in trace or non-trace amounts, near-sonic toroidal velocities, and various collisionality regimes [11, 12, 13, 14]. To validate the use of these simplifications, neoclassical predictions are checked against measured values from plasma discharges [15, 16, 17]. For instance, recent work on DIII-D [14] included a comparison of measured poloidal velocities (based on charge-exchange measurements of fully-stripped C) with those predicted by the neoclassical computer code NCLASS [11]; some agreement was found by retaining strong toroidal rotation effects. The plasmas considered were typically in the banana and intermediate (plateau) regimes.

The high densities attained during H-mode discharges puts C-Mod in a fairly unique position to study the relationship between measurement and neoclassical prediction in a higher collisionality regime than most other tokamaks can attain. The strong gradient region of the pedestal, which is linked to the suppression of turbulence and supports the high densities and temperatures in the plasma core, can be characterized as near or in the Pfirsch-Schlüter (PS) regime for a large fraction of H-mode discharges. Due to the higher collisionalities, the ions, impurities, and electrons are more closely coupled than found in other tokamaks [18, 19]. This coupling enables the evaluation of neoclassical velocity predictions with high spatial resolution in the pedestal region through the use of the impurity (B^{5+}) temperature, T_z, in place of the majority temperature, T_i.

The charge-exchange measurements in the pedestal region provide a good opportunity to test models because of the peaked structure assumed by the edge poloidal velocity profile during all types of H-modes [2]. A few millimeters inside the last closed flux surface, the measured poloidal velocity profile exhibits a sharp peak that is both large, up to 50 km/s, and narrow ($\sim$3 mm at FWHM). These strong gradients in the poloidal velocity are important to study because they are connected to the large radial electric field wells ($|E_r| \lesssim 300$ kV/m) and shearing rates ($\omega_s \lesssim 18$ MHz) found during H-mode operation.

In this study, we focus on the consequences of the radial and parallel, ion and impurity, momentum balance equations which determine the poloidal ion flow, relate the global radial electric field to the toroidal ion flow, and are also responsible for the poloidal variation of the impurity density. Determining the toroidal ion flow (or equivalently, the global radial electric field) from conservation of total toroidal angular momentum in the presence of turbulence is a far more difficult task [20, 21]. No attempt is made in this work to understand radial momentum transport or how the radial electric field is set.

The results of this study show that the neoclassical PS regime prediction of poloidal

velocity match measurement fairly well in the steep gradient region for all collisionality regimes, even when the PS formulation is thought not to apply.

A second important result of this study is derived from the capability to simultaneously measure (at least certain components of) the B^{5+} velocity in the pedestal region at both the high- and low-field sides (HFS and LFS) of the plasma. Based on these measurements and the assumption that certain parameters (u_z and ω_z, discussed below) are constant on a flux surface [12], we infer that there exists an in-out (poloidal) asymmetry in the B^{5+} density in the range of 2–3 (higher at the HFS). This asymmetry is peaked in the radial pedestal region corresponding to the peak in poloidal velocity at the LFS and is in the same direction as the theoretical predictions made for C-Mod [22], although somewhat larger in magnitude.

Section 2 presents the simplified neoclassical theory used in these studies. The methodology, including a description of the charge-exchange diagnostic, is briefly described in section 3. Section 4 explores the neoclassical predictions at the low-field side of the plasma focusing on the poloidal velocities. In section 5 we turn our attention to the high-field side, where the simplest neoclassical predictions fail to match measured parallel velocities. This leads us to infer a poloidal variation in the impurity density, which is explored in section 6. We conclude by discussing these results and the limits of the simplified models used in this study.

2. Neoclassical formalism

Here we briefly review the formalism that we have adopted for this study [8, 9, 12, 23]. Neoclassical flow, to lowest-order, is composed of a component parallel to the magnetic field and a toroidal (ϕ) component. Each part is represented by a coefficient ($u(\psi)$ and $\omega(\psi)$, respectively), which is constant on a flux surface. The total flow on a flux surface is then written as

$$\mathbf{V}_a = u_a(\psi)\mathbf{B} + \omega_a(\psi)R^2\nabla\phi \tag{1}$$

where a denotes the species and $R\nabla\phi$ defines the toroidal direction. One goal of our investigations is to try to understand whether the poloidal pedestal flows in C-Mod are consistent with this lowest-order neoclassical expression. Although poloidal variation of the impurity density due to a *strong* source could alter the form of (1), any radial impurity flow due to a strong source would have to be *exactly* balanced by an ionization-driven ion (or electron) flow, a diffusive flux, or some other anomalous radial ion flow to maintain ambipolarity. For this reason, the possible effect of a strong source is not included in the expressions used in this study. The derivation of the flux functions $u_a(\psi)$ and $\omega_a(\psi)$ can be found in [8, 9, 10, 12] for a single impurity, z. We note here that the derivation of $u_z(\psi)$ depends on the collisionality regime assumed, while $\omega_z(\psi)$, which does not affect the poloidal flows, is determined by the radial force balance and thus includes a term dependent on the radial electric field, E_r. Given that on C-Mod E_r is derived from the CXRS measured velocities, using it to evaluate the neoclassical toroidal

velocity comparison. Thus, we focus solely on predicted poloidal velocities, which are free from this complication.

Defining collisionality as

$$\nu_* = \frac{\nu_{ii} q R}{\epsilon^{3/2} v_{th,i}}, \tag{2}$$

the various transport regimes are given by

$$\begin{aligned} &\text{banana:} && \nu_* < 1 \\ &\text{plateau:} && 1 < \nu_* < \epsilon^{-3/2} \\ &\text{and Pfirsch-Schlüter:} && \nu_* > \epsilon^{-3/2} \end{aligned} \tag{3}$$

Here ν_{ii} is the ion-ion collision frequency, q is the safety factor, ϵ is the inverse aspect ratio, and $v_{th,i}$ is the ion thermal speed.

Taking the poloidal (θ) component of (1) and the definitions of u_z from [12], we construct the following equations for the poloidal impurity velocities when the bulk ions are in the PS and banana collisionality regimes:

$$\begin{aligned} V_{z,\theta}^{\mathrm{PS}} =& \frac{cB_\theta I}{e\langle B^2\rangle}\left(\frac{1}{Zn_z}\frac{\partial p_z}{\partial \psi} - \frac{1}{n_i}\frac{\partial p_i}{\partial \psi}\right. \\ &\left. -1.8\frac{\partial T_i}{\partial \psi}\right) \end{aligned} \tag{4}$$

$$\begin{aligned} V_{z,\theta}^{b} =& \frac{cB_\theta I}{e\langle B^2\rangle}\left(\frac{1}{Zn_z}\frac{\partial p_z}{\partial \psi} - \frac{1}{n_i}\frac{\partial p_i}{\partial \psi}\right. \\ &\left. +\frac{1.18 + 0.70(f_t/f_c)}{1 + 0.46(f_t/f_c)}\frac{\partial T_i}{\partial \psi}\right) \end{aligned} \tag{5}$$

with the fractions of trapped and circulating particles estimated by [23]

$$f_t = 1.46\sqrt{\frac{r}{R}} \qquad \text{and} \qquad f_c = 1 - f_t.$$

Here p is pressure, n is density, T is temperature, and $\mathbf{B} = I\nabla\phi + \nabla\phi \times \nabla\psi$. The preceding equations assume that the poloidal flow has damped to its neoclassical level [24] and consider a trace impurity that is always in the Pfirsch-Schlüter collisionality regime. They also neglect the electron and impurity viscosities, regarding them as small compared with the ion viscosity, and drop electron drag due to the small electron mass. In the C-Mod pedestal, $\epsilon \sim 1/3$, but $\epsilon \ll 1$ is required for a well defined plateau regime. Consequently, to highlight any discrepancies between theory and measurement, we consider only the Pfirsch-Schlüter and banana regime expressions for the flows, but remark that the expression of the plateau regime flow, like that of the Pfirsch-Schlüter regime, has a negative sign for the ∇T_i term [25].

Equations (4) and (5) are written in the limit of $\alpha \equiv Z^2 n_z/n_e \ll 1$. In reality, for the fully-stripped boron population ($Z = 5$), which is used for the CXRS measurements in this study, $\alpha \sim 0.25$. As a result, numerical coefficients used in these equations, which depend on α, should be modified. However, the modifications are expected to be small

and will be neglected herein. For example, increasing α from 0.0 to 0.25 results in a $< 10\%$ increase in the 1.8 coefficient in (4). We also remark that one of the applicability conditions for these equations stated in [12], namely $\alpha \gg (m_i/m_z)^{1/2}(T_z/T_i)^{1/2}$, can be relaxed by replacing $\gg$ with $\gtrsim$ and is therefore satisfied in this study.

3. Methodology

3.1. Experimental Setup

The experimental impurity velocities, temperatures, and densities are derived from charge-exchange recombination spectroscopy (CXRS) measurements at the HFS and LFS of Alcator C-Mod. The resulting spectra from the $n = 7 \rightarrow 6$ transitions (λ =494.5 nm) of B^{4+} are analyzed for their Doppler shift, Doppler width, and brightness giving the desired quantities, v_z, T_z, and n_z, respectively [2]. This analysis becomes difficult near the separatrix and beyond, due to rapidly dropping line brightness as $n_{B^{5+}} \rightarrow 0$. We restrict the data included in this study to those cases that have valid velocity and temperature measurements over the whole range of the B^{5+} poloidal velocity profile. In practice, this means that only H-mode data are included and the peak structure commonly observed near the separatrix in H-mode [2] is well defined (i.e. includes the peak and both sides).

The LFS diagnostic collects the emission from B^{5+} charge-exchanging with H^0 from a diagnostic neutral beam (DNB, 50 keV, 7A) [26]. The poloidal periscope provides 25 views of the midplane with impact radii covering $0.79 < r/a < 1.05$ at $\sim$3 mm radial resolution. The toroidal periscope houses 20 approximately toroidal views covering $0.82 < r/a < 1.07$ at a radial resolution similar to the poloidal periscope. The LFS toroidal periscope view has a small component in the poloidal direction ($\sim 7^\circ$ off the toroidal) whereas the poloidal periscope is aligned to view strictly poloidally.

The HFS CXRS optics collect light from seven approximately toroidal views of the plasma at the midplane near the inner wall of the machine ($0.93 < r/a < 1.05$ at point of tangency with a radial resolution equivalent to $\sim$3 mm at the LFS). The views are angled off of the horizontal plane to be parallel to the local field lines for plasmas with $q_{95} \sim 4.0$; thus the local measurement is approximately of $V_\parallel$ as opposed to V_ϕ. A simple capillary system injects a small amount of room temperature D_2 gas along a major radius and perpendicular to the diagnostic views. The disassociation of D_2 provides the D^0 necessary for charge-exchange interactions. This toroidal localization of the puff leads to a radially localized measurement for each viewing chord. A drawback to this method (compared to the LFS 50 keV diagnostic neutral beam) is that the neutral density, and thus the CXRS signal, drops off much more steeply as a function of the distance inside the separatrix due to the low energy of the D^0 atoms. Thus, we are limited as to how far into the plasma velocities can be measured reliably. A direct assessment of n_B at the HFS is not currently possible due to the lack of information about the injected neutral population and the relevant charge-exchange cross-sections.

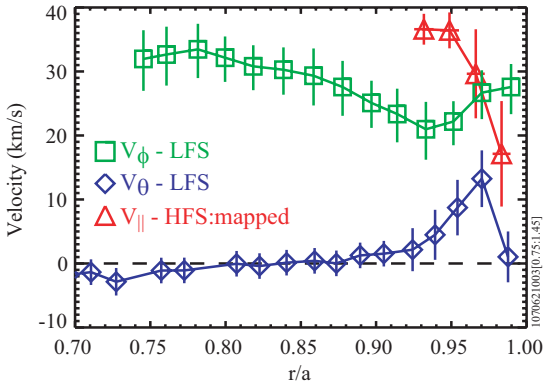

Figure 1. Poloidal (diamonds) and toroidal (squares) velocities measured at the LFS of the plasma on Alcator C-Mod. The parallel velocity measured at the HFS and mapped to the LFS is also shown (triangles).

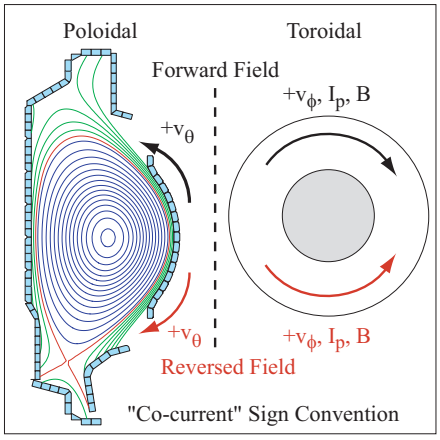

Figure 2. The employed "co-current" sign convention for flows at the low-field side of Alcator C-Mod.

Figure 1 shows representative H-mode velocity profiles derived from all three CXRS periscopes. In the following calculations, and in Figure 1, we have subtracted off the poloidal component from the LFS toroidal measurement, leaving a purely toroidal velocity profile. The poloidal component is typically a very small fraction of the toroidal velocity measurement. The peak in the poloidal velocity and the structure of the HFS velocity profile, shown in Figure 1, are typical for H-mode discharges.

Unless otherwise noted, a positive poloidal velocity indicates flow in the electron diamagnetic direction at the LFS. While the majority of data in this study was obtained from forward-field discharges (positive current, clockwise from above), a few discharges have reversed magnetic fields and currents. Differences between the two discharge types will be noted where significant. Figure 2 shows this choice of sign convention.

3.2. Evaluating T_i and n_i

No direct measurement of either T_i or n_i is available at the plasma edge. However, these values are necessary when evaluating (4) and (5). Thus, we must make some assumptions about the main ion parameters whose characteristics are not directly measured. Specifically, we assume $T_i = T_z$ and $n_i = n_e$. We expect that T_z and T_i are well correlated, based on thermal equilibrium considerations discussed in Appendix A.1. The use of n_e in place of n_i in the following calculations is based on quasi-neutrality. The measurement of n_e (and T_e) in the pedestal region is performed with high spatial resolution by the edge Thomson Scattering (TS) diagnostic [27].

The TS and HFS CXRS profiles are measured at different poloidal locations from the LFS CXRS diagnostic and both sets of data are mapped to the outer midplane using EFIT [28]. The mapping process does not typically align the temperature profiles from these three diagnostics. It has been estimated that the EFIT reconstruction and mapping processes are each only accurate to within a few millimeters.

The question naturally arises as to whether the T_e profile and the low- and high-field side T_z CXRS profiles should be radially aligned or not. First, we expect the B^{5+} temperature to be approximately constant on a flux surface (Appendix A.2). In practice, the shifts needed to align the two T_z profiles have a distribution centered at zero shift with a standard deviation of 1.8 mm, a spread well within the expected variation from EFIT. We therefore feel it is reasonable to radially shift the mapped HFS T_z profiles to match those at the LFS. With respect to the alignment of the electron temperature profile, we show in Appendix A.3 that the measured T_z and T_e profiles are well correlated in terms of their respective pedestal heights and widths. In Appendix A.1 we also examine the thermal equilibration times for T_z and T_e and find that over the region near the top of the pedestal it is reasonable to expect them to be well-correlated. The shift required to align the T_e profile with the LFS T_z profile is, on average, -2.5 mm with a standard deviation of 2.5 mm.

Based on the above arguments and the background found in Appendix A, we have aligned the HFS T_z and TS T_e profiles with the LFS T_z profiles for all data included in this study. The alignment process focuses primarily on aligning the steep gradient regions of the temperature pedestals. The HFS CXRS T_z and TS T_e profiles are shifted radially until the points of steepest gradient (nominally the middles of the pedestals) are at the same location as the steepest gradient in the LFS CXRS T_z profile. For the cases where the LFS profile data is sparse or missing in the steep gradient region, the tops of the pedestals are aligned instead. Section 4.2 provides a sensitivity study of the neoclassical calculations to this mapping and alignment process.

3.3. Evaluating the neoclassical equations

For the calculations in Section 4 we use (4) and (5) to predict velocities at the LFS, *independent* of the measured velocities, thus providing a direct comparison of measurement and model. In Sections 5 and 6 we assume the measured velocities *are*

neoclassical in their variation on a flux surface. We then derive the $u_z(\psi)$ and $\omega_z(\psi)$ constants from the LFS measurements through a rearrangement of the poloidal and toroidal components of (1):

$$u_z(\psi) = \frac{V_{z,\theta}^{\text{meas}}}{B_\theta} \tag{6}$$

$$\omega_z(\psi) = \frac{1}{R}\left(V_{z,\phi}^{\text{meas}} - u_z(\psi)B_\phi\right). \tag{7}$$

Once the flux surface constants are derived, we use them to predict the HFS $V_{z,\|}$ and, after comparison with the measured HFS velocity, to predict the in-out asymmetry in $n_{B^{5+}}$.

4. Comparison of predicted and measured velocities at the LFS

4.1. Poloidal rotation in the steep gradient region

In general, we find many characteristics of measured and predicted poloidal velocity profiles in the pedestal region to be similar. In Figure 3 we present a comparison of typical poloidal velocity profiles (measured and calculated) from one time slice of an H-mode discharge. The prediction for both the PS ($V_{z,\theta}^{\text{PS}}$) and banana ($V_{z,\theta}^{b}$) regime formalisms are shown in Figure 3a. In Figure 3b the components of the PS regime calculation and their sum are displayed. Figure 3c provides the collisionality over the same region. For this example the peak in the poloidal velocity falls near the border between the PS and plateau regimes. It should be noted that although the calculation extends beyond the separatrix ($r/a > 1$) the theory is not valid in that region. However, given the uncertainty in the separatrix location (± 3 mm) we allow the neoclassical predictions to extend into regions of the plasma that may be in the scrape-off layer (SOL).

The $V_{z,\theta}^{\text{PS}}$ profile roughly reproduces the peaking seen in the measured velocity profile. Although the $V_{z,\theta}^{b}$ profile also exhibits some peaking, it has a much smaller peak due to the fact that the ion temperature gradient term is in the opposite direction from the ion pressure gradient term and thus reduces the overall peak magnitude (compare the final terms in (4) and (5)).

Examining the components of the PS regime calculation (Figure 3b and (4)) we see that the peak is composed of two positive peaks, the $\nabla p_i = \nabla(n_e T_z)$ and the ∇T_i terms, and the oppositely directed $\nabla p_z = \nabla(n_z T_z)$ term. It should be noted that the ∇T_i term is determined by ∇T_z and thus the gradient term may be slightly incorrect due to the limited spatial resolution of the CXRS diagnostic and the large uncertainty of the CXRS temperatures at the bottom of the pedestal (due to weak signal there).

In order to gain a more quantitative understanding of the differences between the measured and calculated $V_{z,\theta}$ we have abstracted from each profile in our dataset the position of the poloidal velocity peak, which for the measured profiles we shall call ρ_{peak}. We also have estimated the width and height of the peak in each of the predicted and measured profiles. Included in this dataset are time slices from discharges that exhibit a

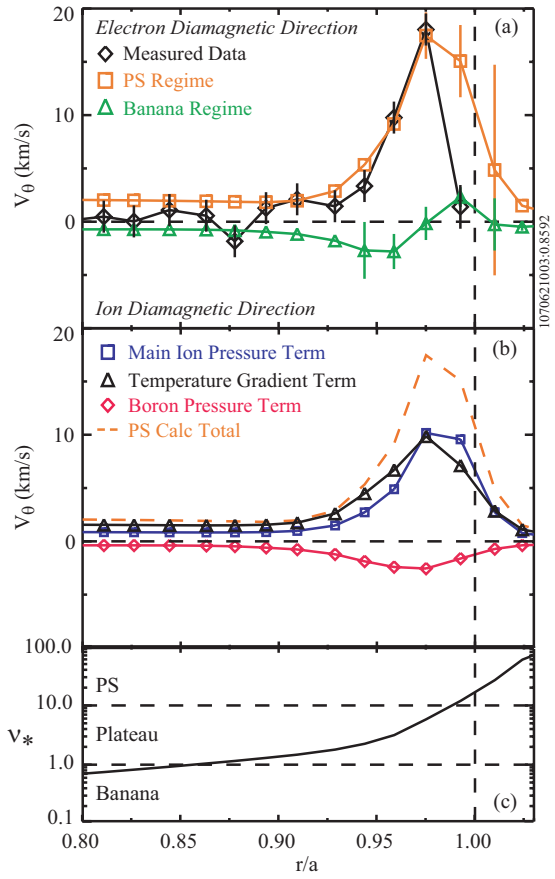

Figure 3. a) Calculated and measured poloidal velocities. b) The three components of the PS regime poloidal velocity calculation. c) The collisionality for the same range.

range of collisionalities at $\rho_{\rm peak}$, from banana to PS. The dataset-averaged width of the peak in $V_{z,\theta}^{\rm PS}$ (4.0 ± 1.0 mm at FWHM) is larger than the dataset-averaged width of the peak in $V_{z,\theta}$ (3.0 ± 1.0 mm at FWHM), but there is no correlation between individual time slices in terms of profile widths or collisionality. On average, the peaks in both the $V_{z,\theta}^{\rm PS}$ and $V_{z,\theta}^{b}$ profiles are slightly shifted radially outward from $\rho_{\rm peak}$.

Figure 4 displays the comparison of the measured $V_{z,\theta}$ peak height to that of both the PS and banana regime calculations for the entire dataset. The height of the peak was measured relative to a baseline velocity determined by the fairly flat velocity profile in the range $0.88 < r/a < 0.93$ (see, for example, Figure 3a). The data is grouped by the collisionality (banana, plateau, or PS) at $\rho_{\rm peak}$. The line representing complete agreement is also shown. We see from this plot that the magnitude of the peak in $V_{z,\theta}^{\rm PS}$ roughly correlates with the magnitude of the measured $V_{z,\theta}$ peak *at all collisionalities.* In contrast, the correlation between the peak value of the measured $V_{z,\theta}$ and that of $V_{z,\theta}^{b}$ is much poorer.

In summary, whether looking at the abstracted profile characteristics (peak height, width, and position) or looking at example profiles, the neoclassical banana regime calculation is a much poorer representation of the measured poloidal velocity profile

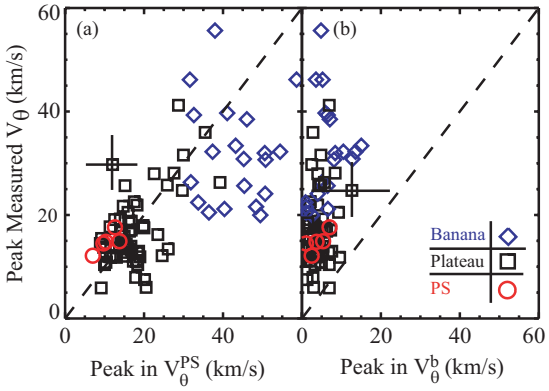

Figure 4. Comparison of peak value of the measured $V_{z,\theta}$ with that calculated using a) the PS regime formalism and b) the banana regime formalism. Lines of perfect agreement are also shown.

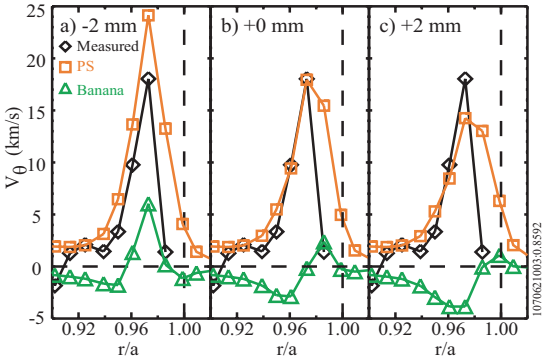

Figure 5. The effect on the neoclassically calculated $V_{z,\theta}$ of shifting the Thomson Scattering profiles another ±2 mm with respect to the LFS CXRS measurements. a) -2 mm. b) +0 mm. c) +2 mm. The symbols are the same as Figure 3a.

in the pedestal region than is the PS regime calculation. Perhaps more surprising is that $V_{z,\theta}^{\rm PS}$ is a fairly good prediction of the measured $V_{z,\theta}$ profile *independent* of the collisionality.

4.2. Sensitivity to the position of the TS profiles

Although we compensate for the variation and uncertainty in the EFIT mapping process by forcing the T_z and T_e profiles to overlay one another, there is still an apparent radial offset between the peaks in the measured and neoclassically calculated poloidal velocity profiles (see Figure 3). This offset leads to the concern that the chosen alignment of the various measured profiles may be incorrect. To address this possibility, we performed the same neoclassical calculations while arbitrarily shifting the TS profiles ±2 mm in relation to the T_z profiles. Figure 5 displays these shifted profiles. We see that +2 mm does not change the position of the peak of the PS regime calculation (within the

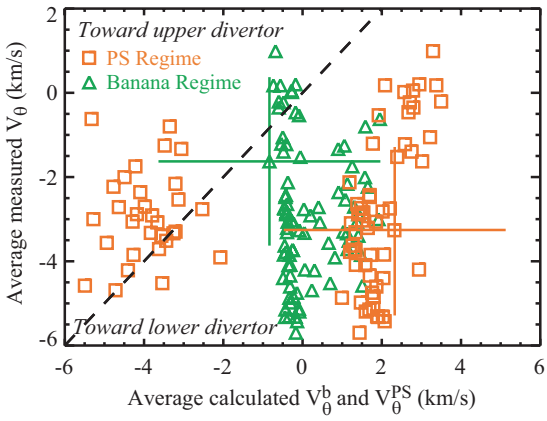

Figure 6. Average V_θ versus average V_θ^{PS} and V_θ^b. The uncertainty of this measurement is quite large compared to the measured value.

resolution) but lowers the magnitude. On the other hand, a shift of -2 mm better aligns the calculated and measured peaks but makes their peak magnitudes moderately to significantly different. The positions of the peaks in the banana regime calculations are shifted similar to those of the PS regime calculations, but the overall magnitudes are still noticeably smaller than the magnitude of the measured peak in all cases. Performing these arbitrary shifts for all the data does not improve the correlation shown in Figure 4.

In summary, it is possible (in individual cases) to *better align* the neoclassical and measured peaks in this manner, but doing so does not enhance, but rather can degrade, the correlation in peak heights presented in Figure 4. A comprehensive study of all predicted profile attributes for all possible radial shifts would likely find shift magnitudes that better correlate the calculated profiles with the measured ones but this would provide only minimal improvement in the correlations presented here.

4.3. Rotation at the top of the pedestal

Shifting our focus further into the core ($r/a < 0.88$) where the collisionality is lower by a factor of 10–15 relative to the collisionality near the separatrix we make a comparison of the measured and predicted poloidal velocities in a region that is entirely in the banana regime. Figure 6 compares the measured poloidal velocity with the predictions from the PS and banana regime formalisms. For this comparison, we averaged the poloidal velocities in the region spanning $0.83 < r/a < 0.88$. For clarity, the data is presented as flowing toward the upper or lower divertors, regardless of magnetic field direction. There is no clear correlation between experiment and either model for the current dataset. It should be noted that the uncertainty in the measured poloidal velocities is ±2–3 km/s. Because this is an absolute measurement rather than a relative one (such as the height of the peak) concerns about calibration of the diagnostic must be considered. For example, a small shift in the wavelength calibration (e.g. 0.05 Å) would shift all the points up,

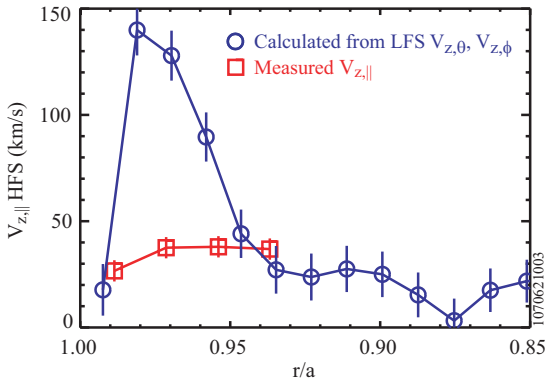

Figure 7. The calculated HFS parallel velocity (circles) determined by the $u_z(\psi)$ and $\omega_z(\psi)$ that were derived from the LFS velocities. Also shown is the HFS CXRS velocity measurement (squares).

or in the direction of "toward the upper divertor," by ∼3 km/s.

5. Neoclassical prediction of HFS velocities

The second emphasis of this study is the comparison of the high- and low-field side B^{5+} velocities with neoclassical predictions for the variation of $\mathbf{V}$ on a flux surface. As discussed in Section 3, the CXRS measurements at the HFS do not extend as far inside the separatrix as do those at the LFS. Thus, our comparisons are limited to the region near $\rho_{\rm peak}$, the location of the peak poloidal flow.

We begin the analysis by determining $u_z(\psi)$ and $\omega_z(\psi)$ from the LFS CXRS data through (6) and (7). Then, assuming they are constant on a flux surface, we use the magnetic reconstruction provided by EFIT (and the extra shift that aligns the impurity temperature profiles) to map these flux coefficients to equivalent locations at the HFS. Together with the known viewing angle of the HFS periscope, we generate an expected $V_{z,\|}$ at the HFS of the plasma which can be compared to the directly measured $V_{z,\|}$. An example comparison is shown in Figure 7. The predicted parallel velocity calculated in this manner has a peaked structure driven by the LFS poloidal velocity contribution to $u_z(\psi)$. We see that the measured parallel velocity in the region within 1 cm inside the separatrix is lower than the prediction by a factor of up to 6. Furthermore, the largest measured velocities are at a different radial location than the peak of the calculated profile. Often the measured profile does not show a complete peak (if it indeed peaks at all) in the region sampled by the diagnostic.

6. Poloidal variation of impurity density

One possible explanation of the discrepancy between the directly measured $V_{z,\|}$ and that generated from the $u_z(\psi)$ and $\omega_z(\psi)$ derived at the LFS is that we are using a somewhat simplified model of $\mathbf{V}$ in (1) when considering multiple poloidal locations.

An underlying assumption in (1), (6), and (7) is that the impurity density is constant on a flux surface. Prior studies on C-Mod, both experimental [29, 30, 31] and theoretical [22], have identified the potential for up-down and in-out asymmetries. In the theoretical model [22], the variation in impurity density is driven by friction between the impurities and the majority ions in poloidally varying fields.

In-out asymmetries in the impurity density have also been inferred on other tokamaks as well. For example, on JET, near-sonic toroidal flows driven by unbalanced neutral beam injection cause a centrifugal force that pushes impurities to the low-field side of the tokamak [32, 33]. Similar centrifugal effects also were observed for heavy impurities on the ASDEX Upgrade tokamak [34]. When JET removed the neutral beam heating and only used ICRF sources to heat optimal shear plasmas, tomographic reconstruction of nickel emission indicated a minor density build up at the high-field side of the plasma. It should be noted that these studies were more focused on the core plasma rather than the pedestal region.

In this section we will allow n_z to vary on a flux surface and calculate the impurity density asymmetry required to make the measured velocities at both sides of plasma consistent with a modified form of (1).

6.1. Modification of the neoclassical equations

Allowing the impurity density to vary poloidally has a simple but profound effect on the first-order flow equation. There is no modification to the last term in (1) as it is purely toroidal. The impurity density, $n_z(r,\theta)$, once absorbed into the constant $u_z(\psi)$ during the neoclassical derivation is no longer constant over the flux surface and must be considered separately. For clarity we will relabel the new flux constant $k_z(\psi)$. The modified equation for the impurity velocity becomes (for $Z \gg 1$) [22]

$$\mathbf{V}_z = \frac{k_z(\psi)}{n_z(r,\theta)}\mathbf{B} + \omega_z(\psi)R^2\nabla\phi. \tag{8}$$

With this modification, we can now use the measured velocities to calculate the impurity density at the HFS of the plasma. First, we determine the impurity density profile at the LFS midplane from the measured CXRS brightnesses [2] and use those values to calculate $k_z(\psi)$ and $\omega_z(\psi)$ for the flux surfaces in the pedestal region. The flux constant $k_z(\psi)$ is given by

$$k_z(\psi) = \frac{n_{z,\mathrm{L}}^{\mathrm{meas}}}{B_{\theta,L}} V_{z,\theta,\mathrm{L}}^{\mathrm{meas}}, \tag{9}$$

where L (H) indicates values from the LFS (HFS), and $\omega_z(\psi)$ is still determined through (7) (replacing u_z with k_z/n_z). Taking the component of the velocity parallel to the total

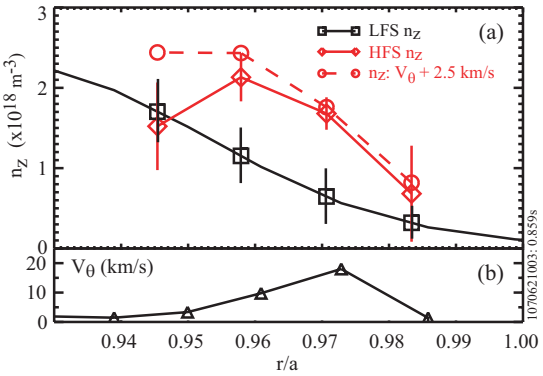

Figure 8. a) The measured LFS impurity density (squares) and the calculated HFS impurity density (diamonds, mapped to LFS). Also shown is the calculated HFS impurity density if we arbitrarily increase the poloidal velocity by 2.5 km/s (circles). b) The LFS poloidal velocity profile, reproduced for reference.

magnetic field at the HFS we find

$$\begin{aligned} V_{z,\parallel,\mathrm{H}} &\equiv \mathbf{V}_{z,\mathrm{H}} \cdot \hat{b} \\ &= \left(\frac{k_z(\psi)}{n_{z,\mathrm{H}}} \mathbf{B}_{\mathrm{H}} + \omega_z(\psi) R_{\mathrm{H}}^2 \nabla\phi \right) \cdot \hat{b} \\ &= \frac{k_z(\psi)}{n_{z,\mathrm{H}}} B_{\parallel,\mathrm{H}} + \omega_z(\psi) R_{\mathrm{H}} \cos\zeta \end{aligned} \tag{10}$$

where $\hat{b}$ is a unit vector in the magnetic field direction and ζ ($\sim 10°$) is the angle that the magnetic field makes with the toroidal direction ($\cos\zeta \equiv B_{\phi,H}/B_{\parallel,H}$). Mapping the flux constants to the HFS we now assume the measured HFS parallel velocity is the left hand side of Equation 10 and solve for $n_{z,\mathrm{H}}$.

The resultant HFS and LFS impurity density profiles are plotted together (given the mapping as determined by EFIT and the T_z profiles) versus normalized minor radius in Figure 8. This plot is typical of H-mode results for Alcator C-Mod. The HFS densities for the points furthest into the plasma (near the top of the pedestal) are close to or lower than the LFS density on the same flux surface. For flux surfaces in the steep gradient pedestal region the HFS densities are significantly higher than their LFS counterparts. The uncertainties on the HFS densities shown in Figure 8 are only from the uncertainties in the measured velocities and do not include the significant uncertainty of the LFS density calculation.

The comparison of HFS and LFS n_z can be simplified by reorganizing (8)–(10) in terms of a density asymmetry,

$$\begin{aligned} \mathrm{A} &\equiv \frac{n_{z,\mathrm{H}}}{n_{z,\mathrm{L}}} \\ &= \frac{V_{z,\theta,\mathrm{L}} \frac{B_{\parallel,\mathrm{H}}}{B_{\theta,\mathrm{L}}}}{\Delta_\parallel + \alpha V_{z,\theta,\mathrm{L}} \frac{B_{\phi,\mathrm{L}}}{B_{\theta,\mathrm{L}}} \cos\zeta} \end{aligned} \tag{11}$$

where $\alpha = R_{\rm H}/R_{\rm L}$ and

$$\Delta_{\|} \equiv V_{z,\|,{\rm H}} - \alpha V_{z,\phi,{\rm L}} \cos\zeta. \tag{12}$$

The asymmetry is preferable to a direct calculation of $n_{z,{\rm H}}$ because it is only a function of the measured velocities and eliminates the dependence on the LFS density calculation. Equation (11) properly reduces to unity if one uses (12) along with $\cos\zeta \equiv B_\phi/B_\|$ while assuming no poloidal variation in B and R (cylindrical limit). Finally, we see by the form of (11) that the asymmetry information is carried primarily in $V_{z,\theta}$. For example, if $V_{z,\theta} \to 0$ over the flux surface, then the flow at both sides of the plasma would be purely toroidal, varying only with radius (assuming ω constant on a flux surface). In that situation, $\Delta_\| \to 0$ and A is undefined.

6.2. Inferred asymmetry

An asymmetry factor is calculated at each radial location corresponding to a valid HFS CXRS measurement, resulting in several values from a single time slice. Figure 9a–c displays the derived asymmetries for the entire dataset as a function of the distance from $\rho_{\rm peak}$ ($x \equiv R - \rho_{\rm peak}$), which is a well defined location being determined from the same CXRS diagnostic. Using this distance was found preferable to using the separatrix location because of the higher uncertainty in the separatrix location. The separatrix is typically 2–3 mm beyond the poloidal velocity peak and is shown as a shaded region. Figure 9a shows the asymmetry from all available data points. We see that even within the large scatter in the data, there is a trend towards larger asymmetry in the region of the poloidal velocity peak ($x \sim 0$). Figures 9b and 9c are binned averages of the dataset separated by forward field and reversed field respectively. Note that the uncertainties shown for binned data are the weighted standard deviation of data about the mean for each averaged set of data (as opposed to the direct uncertainty in the underlying measurement, which is generally smaller, especially near $x = 0$).

In all cases, we find that the asymmetry increases near $\rho_{\rm peak}$. The in-out asymmetry is consistently a factor of 2–3 in the region near $x = 0$. Moving into the plasma ($x < 0$) the asymmetry drops to order unity supporting the expectation that the asymmetry correlates with increased poloidal velocity. Beyond the peak towards the separatrix ($x > 0$), both the collected CXRS signal and the associated measured velocities drop significantly and the uncertainties become large, making it difficult to determine the magnitude of the asymmetry. Comparing the binned data of Figures 9b and 9c, we see that reversed field discharges appear to have higher asymmetries than do forward field ones, correlating with the higher poloidal velocities found during those discharges.

We also see in Figure 9a that the uncertainty in A decreases near $\rho_{\rm peak}$. Taking the derivative of Equation 11 with respect to $V_{z,\theta}$, we infer that the *total uncertainty* in A is (to lowest order) inversely proportional to the magnitude of the poloidal velocity. This effect can be seen by the increase in the magnitude of the uncertainty as we move away in either direction from the location of the peak in the poloidal velocity.

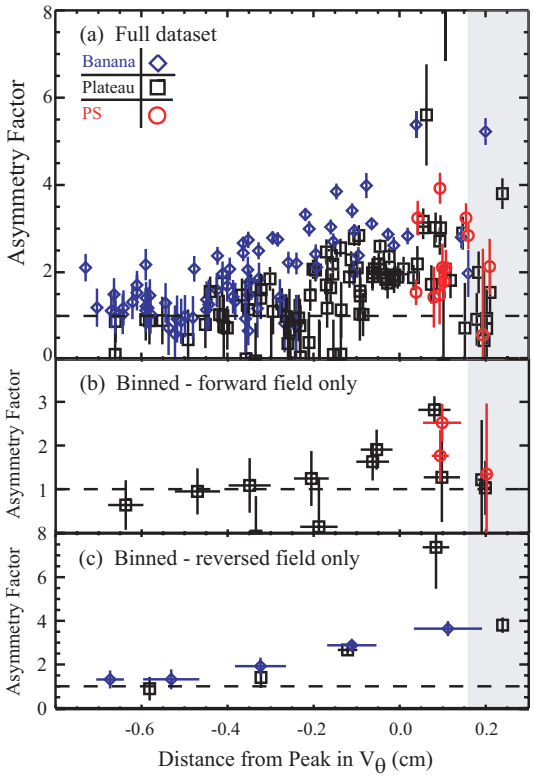

Figure 9. a) The asymmetry for the entire dataset separated by collisionality. b–c) Binned averages for just the forward and reversed field portions of the dataset.

It is also educational to plot the asymmetry, A, versus $V_{z,\theta}$ as we have done in Figure 10a. For reference, we provide representative $V_{z,\theta}$ profiles from forward and reversed field discharges in Figure 10b. The data is separated into four regions based on the distance from ρ_{peak}. As stated earlier, the data from Region III near ρ_{peak} have the lowest uncertainties and thus we have the most confidence in them. Due to the larger number of data points, we have deviated from the standard sign convention and defined positive poloidal velocities as those flowing toward the upper divertor at the LFS, regardless of field direction. As expected, the highest asymmetries are at the highest poloidal velocities and we see that there is a strong correlation between these two values. This trend is well described by the form of Equation 11 if we assume that $\Delta_{\|}$ is a constant. This is not a natural assumption, yet it is roughly true for a majority of the data (not shown).

Neoclassical derivations of the impurity density, which are explored in the following section, do not provide any mechanism for obtaining values of $A < 1$. However, we see in Figure 10 that there is a significant number of data points in this region, with a strong correlation to $V_{z,\theta}$. As mentioned before, as $V_{z,\theta} \rightarrow 0$ the flow becomes purely toroidal and our technique for measuring the asymmetry fails. These concerns are addressed further in Sections 6.4 and 7.2.

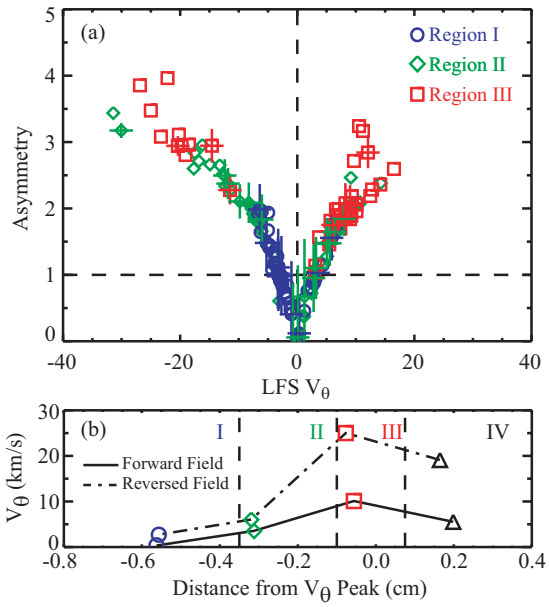

Figure 10. a) The dependence of the asymmetry on measured LFS poloidal velocity in the steep gradient region. Data from Region IV (see Fig. 10b) are not plotted due to the large uncertainties associated with that data. b) Typical LFS V_θ profiles for forward and reversed fields. The regions used in Fig. 10a are also indicated.

6.3. Neoclassical prediction of impurity density asymmetry

For comparison to the asymmetries inferred from the measured velocities, we utilize a formalism by Fülöp and Helander that predicts poloidal density asymmetries based only on the measured pressure profiles [22]. As stated before, the build up of impurity density at the HFS is driven by friction between the impurities and the majority ions in poloidally varying fields, rather than by a centrifugal force, which would cause a higher density at the LFS. Here, we apply their work to the present C-Mod dataset and show that the predicted asymmetries are of the same form (peaked at the HFS and similar magnitude) as found above.

Equation 27 in [22] describes the poloidal distribution of the normalized impurity density, $n = n_z/\langle n_z \rangle$, assuming trace impurities in a strongly collisional plasma. Expanding that equation in terms of g^{-1}, where

$$g = -\frac{m_i n_i I}{e\tau_{iz} n_z \langle \mathbf{B}\cdot\nabla\theta\rangle}\left(\frac{\mathrm{d}\ln n_i}{\mathrm{d}\psi}\right) \tag{13}$$

measures the steepness of the bulk ion density profile, they find a limiting form for the zeroth-order ($n = n_0 + n_1 + O(g^{-2})$) impurity density,

$$n_0 = \frac{\gamma}{1 - \langle (1+\gamma b^2)^{-1}\rangle}\frac{b^2}{1+\gamma b^2}. \tag{14}$$

Here $\gamma \equiv 2.8(\ln T_i)'/(\ln n_i)'$ (where prime denotes a derivative with respect to ψ), τ_{iz} is the ion-impurity collision time, and $b \equiv B/\langle B^2\rangle^{1/2}$. In the cylindrical limit ($b = 1$), n_0

becomes a flux function, as expected. For C-Mod, g peaks sharply in the steep gradient region and is higher on average in plasmas with higher collisionality. For medium and low collisionality discharges $g = 5.3 \pm 3.1$ at $\rho_{\rm peak}$, while in higher collisionalities g ranges anywhere between 10–40. Thus, (14) is a valid approximation for most of the edge region. The value of γ also varies significantly at the location of the steepest gradient, with an average value of $\gamma = 3.7 \pm 3.1$, though larger values are observed. Evaluating (14) at both sides of the plasma we find that the impurity density builds up near the inner wall, where the magnetic fields are higher. This gives an expected asymmetry of $\mathrm{A}_0 \equiv n_{0,\mathrm{H}}/n_{0,\mathrm{L}} = 1.5 \pm 0.3$ (for local values of γ), somewhat lower than that inferred from the velocity data.

6.4. Sensitivity to the poloidal velocity

Given the large variation in the derived density asymmetry shown in Figure 9 for $x < 0$ (towards the center of the plasma) and the expectation that all A should be greater than 1, we have investigated the sensitivity of the derived asymmetry to possible errors in the magnitude of $V_{z,\theta}$. As shown in Figure 1, for $r < \rho_{\rm peak}$, $V_{z,\theta}$ is near zero or negative. In Figure 8 we show the response of the inferred HFS impurity density to an arbitrary increase in $V_{z,\theta}$ of 2.5 km/s, which is the level of uncertainty for the velocity measurement as well as a reasonable magnitude for a potential systematic error due to miscalibration. We see that farthest from the separatrix, where the poloidal velocity is naturally near zero, such a small change in poloidal velocity has a significant effect on the asymmetry—where the asymmetry was originally approximately unity, it has now become greater than one. On the other hand, there is little change in the inferred asymmetry to the poloidal velocity at other points in the profile, particularly near $\rho_{\rm peak}$.

The effect on the asymmetry of a systematically low $V_{z,\theta}$ can also be evaluated through (11) and Figure 10. The largest effect will be where the poloidal velocities are smallest, which is where $\mathrm{A} \leq 1$. In fact, a change of just 2.5 km/s will significantly increase the smallest asymmetries, moving most points above the $\mathrm{A} = 1$ line (not shown). The change in A is less noticeable where $V_{z,\theta}$ is large (of order 10–20%) and all the data continues along the same A versus $V_{z,\theta}$ trend shown in Figure 10.

7. Discussion

7.1. Limits of the results

An unexpected result of this work is the strong correlation between the PS regime predictions and the measured poloidal velocity near the separatrix for all collisionalities. It is natural to assume that the banana regime formalism would have better predicted the velocities measured for the lowest collisionality discharges, but this appears not to be the case. One factor which makes the banana regime calculation a poorer match to the data is that the main ion temperature gradient term is of opposite sign and nearly the same magnitude as the main ion pressure gradient term (recall (5)). Of course, at

low collisionalities there will be some portion of the majority species which is colder, and thus more collisional, and accounting for this could have some small effect on the ∇T_i term in (5). However, even though these slow ions by themselves might drive flows similar to those in the Pfirsch-Schlüter formalism, their effect is overwhelmed by the oppositely directed contribution from ions with $m_i v^2/2T_i > 4/3$. Additionally, recent theoretical work has discovered a much stronger modification to the banana regime expression due to radial electric field effects in the steep gradient region [35]. That recent work shows that the coefficient on the ∇T_i term is reduced from its value in (5) and can even change the sign, depending on the strength of the radial electric field. Reducing the effect of the ∇T_i term would result in an increase in the magnitude of the peak in the $V^b_{z,\theta}$ profile. However, without changing sign such an effect is insufficient to make the calculated profiles well-correlated with the measured profiles.

Most of the profiles included in this dataset are actually in the plateau regime at ρ_{peak}. Furthermore, except for the lowest collisionality discharges, a portion of every velocity profile is in the plateau regime. It is possible to develop neoclassical equations similar to (4) and (5) for the plateau regime. Predictions from these equations would be better suited for comparison to a large fraction of the measured velocity profiles used in this study. This process is beyond the scope of this paper, though it is recommended that such a set of equations be developed for future studies.

In this study we have not attempted to isolate the role of poloidally localized boron sources on measured in-out asymmetries or the effect of radial impurity transport. We believe that further experiments, such as those that vary the relative magnitudes of the HFS and LFS boron sources, are required to determine if these concerns have an effect on the derived asymmetry.

7.2. Limit of first-order theory

Here, we highlight a few limitations of the models used to predict the poloidal velocities and impurity density asymmetries. The first-order theory used to predict $V_{z,\theta}$ is derived in a limit where $\delta_i \equiv \rho_p/L_\perp \ll 1$, where ρ_p is the poloidal ion gyroradius and $L_\perp$ is the perpendicular pressure scale length. For the steep gradient region in C-Mod, we find $1 < \delta_i < 5$ for the main ions, which violates this assumption. This means the ion banana orbits extend across a significant portion of the pedestal allowing trapped particles to sample potentially significantly different regions of the plasma. Thus, we are concerned about the applicability of the banana regime formulation in [12] to the lowest collisionality C-Mod data. The magnitude of the error that this violation causes is not readily quantified, but large changes in poloidal flow are possible due to the radial electric field in the pedestal [35].

Another assumption integral to the derivation of first-order theory and the asymmetry calculation is that ω_z is a constant on a flux surface. If ω_z is not constant then, of course, the derived asymmetry will be changed.

8. Summary

We have presented a comparison of neoclassically calculated poloidal velocity profiles with those from the CXRS diagnostic on Alcator C-Mod. Velocity profiles were predicted using poloidal flow equations in both the Pfirsch-Schlüter and banana regimes. In the steep gradient region the height, position, and width of the measured poloidal velocity peak were compared to those of the predictions. The values were similar for location and width, within the uncertainties of the measurements and calculations. On average, the predicted peaks were both slightly wider and located at larger major radii than those of the measured profiles. Better agreement was found between the peak heights of the measured and PS regime formalism profiles, regardless of the actual collisionality of the plasma. In contrast, the magnitude of the profile peak predicted using the banana regime formalism had a much poorer correlation with measured peak heights, even for the lowest collisionality plasmas considered.

After determining flux surface constants from the LFS measured poloidal and toroidal velocities, we then constructed predicted $V_{\|}$ profiles at the HFS of the plasma. When compared with the profiles actually measured at the HFS, these predicted profiles had significantly different magnitudes and shapes. This led us to relax an assumption typically used in neoclassical theory and allow poloidal variation in the impurity density. Using this modified model, we calculated the ratio of HFS to LFS n_z necessary to make the measured velocities from both sides of the plasma consistent under the assumed formalism. The inferred asymmetry of 2–3 at the location of the peak in the poloidal velocity, is similar to the predicted asymmetry of 1–2 found in previous numerical studies of C-Mod data.

Acknowledgments

The authors would like to thank the C-Mod Operations team and the Plasma Science and Fusion Center administration team for all their hard work which made this research possible. Additional thanks go to W.M. Burke, R.M. Churchill, R.S. Granetz, P. Helander, I.H. Hutchinson, J.W. Hughes, G. Kagan, S.M. Wolfe, S.J. Wukitch and D.G. Whyte for their help, efforts, and insight. This work was funded by DOE award #DE-FC02-99ER54512.

Appendix A. Profile alignment

In light of the uncertainty in the mapping process and the sensitivity of neoclassically calculated profiles to the relative locations of the measured profiles, we consider whether or not the various temperature profiles should be aligned after mapping to the LFS midplane. Figure A1a shows the relevant temperature profiles from a single time during a strong H-mode. The profiles are rather similar, yet are separated by $\sim$3 mm. After forced alignment there is very good agreement between the temperature profiles, as seen

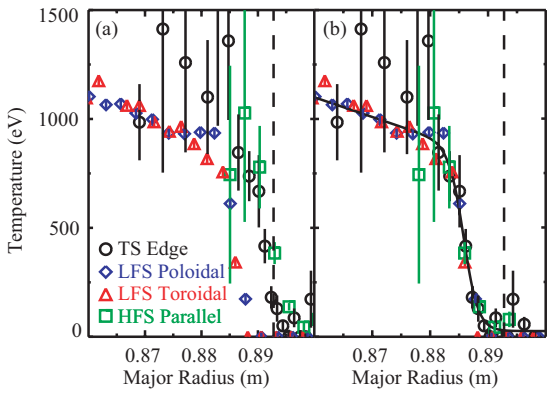

Figure A1. An example of a) the unshifted and b) the shifted impurity and electron temperature profiles. The fit to the CXRS data is also shown.

in Figure A1b.

Appendix A.1. Thermal equilibration

Here we review the thermal equilibration times between the various species in order to support radially shifting the temperature profiles and the use of the approximation that $T_i \sim T_z$. Values for all the relevant time scales are collected in Figure A2 for a typical H-mode. The time it takes the boron impurity to thermally equilibrate to the main ion species (in ms) is [36]

$$\tau_{zi} = 5.56 \times 10^{27} \frac{(m_i T_z + m_z T_i)^{3/2}}{(m_i m_z)^{1/2} Z^2 n_i \lambda_{zi}}. \tag{A.1}$$

Here, the units of temperature are eV, density is in m^{-3} and λ_{zi} is given by

$$\lambda_{zi} = \ln(\Lambda_{zi}) \sim 17.3 - \frac{1}{2}\ln(\frac{n_i}{10^{20}}) + \frac{3}{2}\ln(\frac{T_i}{1000}). \tag{A.2}$$

Similar estimates can be made of the boron-electron (τ_{ze}) and ion-electron equilibration (τ_{ie}) times. All three profiles are shown in Figure A2 for a single time-slice in a typical discharge.

Over much of the pedestal, the thermal equilibration between B^{5+} and the bulk ions is found to be much faster than the energy transport time, which we define as

$$\tau_{\mathrm{trans}} \equiv L_{p,i}^2/\chi. \tag{A.3}$$

χ is the thermal diffusivity and $L_{p,i}$ is the ion pressure scale length. χ is approximated by

$$\chi \equiv \frac{P_{\mathrm{flux}}}{\frac{3}{2} n \nabla (T_i + T_e)} \tag{A.4}$$

where P_{flux} is the total power crossing the last closed flux surface. τ_{ze} is slightly longer than τ_{zi} but still much shorter than the energy transport time. We also find that τ_{ie} is shorter than τ_{trans} over much of the plasma but in the pedestal the two become

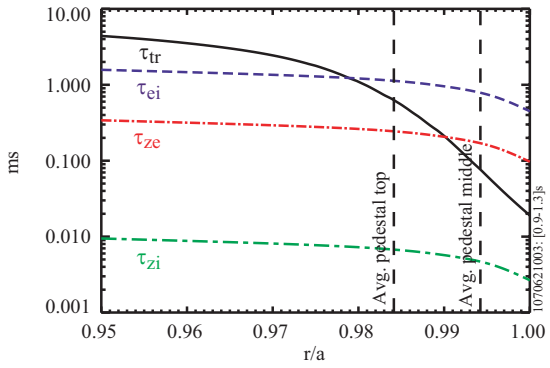

Figure A2. The equilibrium and diffusivity times in the pedestal region for a typical discharge.

approximately equal. Although this might lead us to expect the ions and electrons are generally decoupled in this region, the full energy balance equation should be considered to properly resolve that question.

We conclude that T_z is a reasonable approximation for T_i in the pedestal region given that τ_{zi} is less than all other equilibrium times and much less than τ_{trans} over most of that region. However, we reiterate that the comparison of equilibrium times is not a rigorous proof. We should also point out that to evaluate (A.1) we must make the same assumption that we are trying to validate, namely $T_i \sim T_z$. However, even if we used $T_i \sim 1.5T_z$ the general results are still the same. The relative magnitudes of the equilibrium times also provide good evidence for the correlation found in Figures A1b and A4.

Appendix A.2. Alignment of HFS data

Here we address the forced alignment of the HFS CXRS T_z measurements to those at the LFS. This alignment assumes T_z is constant on a flux surface which follows from the work of Fülöp and Helander [22]. Working in the Pfirsch-Schlüter regime and assuming that the impurity density is much smaller than the ion density, they calculate the first order correction to the main ion temperature, which is assumed nearly constant on a flux surface, from

$$\nabla_{\|} T_i = \frac{16}{25} \frac{I T_i}{\Omega_i \tau_i} \frac{\mathrm{d} \ln T_i}{\mathrm{d}\psi} \left(1 - \frac{B^2}{\langle B^2 \rangle} \right). \tag{A.5}$$

Here, Ω_i is the ion cyclotron frequency and τ_i is the ion collision time. We see that the parallel gradient of T_i involves the radial flux gradient of T_i as well as the strength of the magnetic field. Integrating along a field line from the low- to high-field sides we find, for typical C-Mod parameters, that this correction is only a few percent for flux surfaces outside the midpoint of the pedestal and that this correction rapidly decreases as one moves into the plasma. Thus, we feel confident aligning the LFS and mapped HFS B^{5+} temperature profiles with radial shifts.

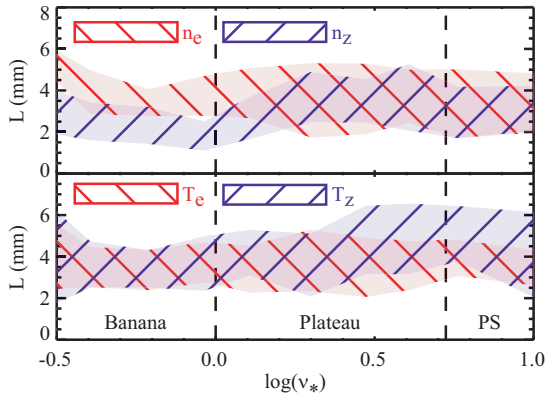

Figure A3. Comparison of the electron and boron density and temperature pedestal scale lengths.

Appendix A.3. T_e and T_z profiles

To further motivate shifting the mapped TS profiles to match those from the LFS CXRS diagnostic, we examine several characteristics of the measured T_e and LFS T_z profiles. The method we employ for abstracting profile characteristics is to fit each set of pedestal data with a hyperbolic tangent (tanh) function that is connected at the top of the pedestal to a linear fit of the core data [37]. The combined form of this fit (f) depends on five parameters that are allowed to vary during the fitting process: the slope of the linear portion (m) and the height (h), base level (b), midpoint (r_0), and half width (Δ) of the pedestal.

$$f(r) = \frac{h}{2}\left(\frac{\tanh(r_0 - r)}{\Delta} + 1\right) + b + (r_0 - \Delta - r)mH(r_0 - \Delta - r) \tag{A.6}$$

where $H(r_0-\Delta-r)$ is the Heaviside step function which turns on for values of $r < r_0-\Delta$. With these fits, we may systematically derive pedestal heights and widths as well as calculate smooth gradients. The tanh fit to the impurity temperatures is shown for the data in Figure A1b.

The first profile characteristic we explore is the radial scale-length, L, which may remain constant even as the pedestal height and width changes. It turns out that the scale lengths of the temperature and density profiles, both for the electrons and the B^{5+} impurity, are fairly constant over the range of H-mode discharges considered. Furthermore, they are all of the same order. Figure A3 shows all the temperature and density scale lengths measured in the pedestal region plotted against the collisionality at the location of the maximum profile gradient.

Next we examine the magnitude of both the T_e and T_z pedestals and find that in C-Mod they are well correlated from the top to the separatrix. Figure A4a shows a comparison of T_e and T_z at the top of the pedestal (based on the tanh fits). The same strong correlation between T_z and T_e continues through middle of the pedestal

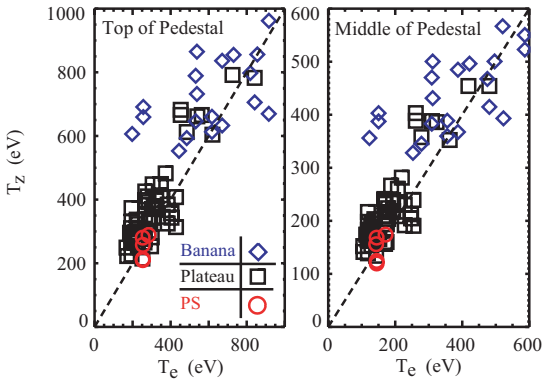

Figure A4. Comparison of the electron temperature to the B^{5+} impurity temperature at a) the top of the pedestal and b) the steep gradient region.

as shown in Figure A4b. In contrast, lower density/collisionality tokamaks can observe that the electron and ion temperatures are less correlated in the edge region [38]; T_i drops more slowly than T_e moving out through the pedestal to the SOL. For those machines, $L_{T,z}$ can be much larger than $L_{T,e}$. We note that the C-Mod data spans a range that includes lower collisionalities where we might not expect T_z and T_e to be so closely correlated/coupled, but they still are.

Finally, we note that, even in an otherwise constant discharge, the difference between the locations of the pedestal midpoints (for T_z, T_e) can swing from positive to negative and back. The variation in radial difference tends to be in the range of 1–3 mm, but can be larger depending on the shape of the equilibrium.

Because the general profile characteristics are well matched and the variation in relative location of the CXRS and TS profiles is similar to the expected EFIT uncertainty it seems reasonable to assume that the T_z and T_e profiles should overlay each other.

References

[1] Biglari H, Diamond P H and Terry P W 1990 *Physics of Fluids B: Plasma Physics* **2** 1–4
[2] McDermott R M *et al.* 2009 *Physics of Plasmas* **16** 056103
[3] Burrell K H 1997 *Physics of Plasmas* **4** 1499
[4] Terry P W 2000 *Rev. Mod. Phys.* **72** 109–165
[5] Ida K, Hidekuma S, Miura Y, Fujita T, Mori M, Hoshino K, Suzuki N, Yamauchi T and Group J M 1990 *Phys. Rev. Lett.* **65** 1364–1367
[6] Andrew Y *et al.* 2008 *EuroPhysics Letters* **38** 15003
[7] Groebner R J, Burrell K H and Seraydarian R P 1990 *Phys. Rev. Lett.* **64** 3015–3018
[8] Kim Y B, Diamond P H and Groebner R J 1991 *Physics of Fluids B: Plasma Physics* **3** 2050–2060
[9] Hirshman S P and Sigmar D J 1981 *Journal of Nuclear Fusion* **21** 1079
[10] Hinton F L and Hazeltine R D 1976 *Reviews of Modern Physics*
[11] Houlberg W A, Shaing K C, Hirshman S P and Zarnstorff M C 1997 *Physics of Plasmas* **4** 3230–3242
[12] Catto P J and Simakov A N 2006 *Physics of Plasmas* **13** 052507
[13] Belli E A and Candy J 2009 *Plasma Physics and Controlled Fusion* **51** 075018 (22pp)

[14] Wong S K, Chan V S and Solomon W M 2008 *Physics of Plasmas* **15** 082503
[15] Solomon W M, Burrell K H, Andre R, Baylor L R, Budny R, Gohil P, Groebner R J, Holcomb C T, Houlberg W A and Wade M R 2006 *Physics of Plasmas* **13** 056116
[16] Stacey W M 2002 *Physics of Plasmas* **9** 3874–3883
[17] Scarabosio A, Bortolon A, Duval B P, Karpushov A and Pochelon A 2006 *Plasma Physics and Controlled Fusion* **48** 663–683
[18] Thomas D M, Leonard A W, Osborne T H, Groebner R J, West W P and Burrell K H 2006 *Plasma Physics and Controlled Fusion* **48** A183–A191
[19] Loarte A *et al.* 2004 *Physics of Plasmas* **11** 2668–2678
[20] Catto P J, Simakov A N, Parra F I and Kagan G 2008 *Plasma Physics and Controlled Fusion* **50** 115006 (21pp)
[21] Parra F I and Catto P J 2009 *Plasma Physics and Controlled Fusion* **51** 095008 (38pp)
[22] Fulop T and Helander P 2001 *Physics of Plasmas* **8** 3305–3313
[23] Helander P and Sigmar D J 2002 *Collisional Transport in Magnetized Plasmas* Cambridge University Press, Cambridge
[24] Morris R C, Haines M G and Hastie R J 1996 *Physics of Plasmas* **3** 4513–4520
[25] Hazeltine R D 1974 *Physics of Fluids* **17** 961–968
[26] Korepanov S A *et al.* 2004 *Review of Scientific Instruments* **75** 1829–1831
[27] Hughes J W, Mossessian D A, Hubbard A E, Marmar E S, Johnson D and Simon D 2001 *Review of Scientific Instruments* **72** 1107–1110
[28] Lao L L, Ferron J R and Groebner R J 1990 *Journal of Nuclear Fusion* **30** 1035
[29] Pedersen T S, Granetz R S, Marmar E S, Mossessian D, Hughes J W, Hutchinson I H, Terry J and Rice J E 2002 *Physics of Plasmas* **9** 4188–4192
[30] Rice J, Terry J, Marmar E and Bombarda F 1997 *Nuclear Fusion* **37** 241–9
[31] Reinke M L and Hutchinson I H 2008 AIP volume 79 10F306
[32] Chen H, Hawkes N C, Ingesson L C, von Hellermann M, Zastrow K D, Haines M G, Romanelli M and Peacock N J 2000 *Physics of Plasmas* **7** 4567–4572
[33] Romanelli M and Ottaviani M 1998 *Plasma Physics and Controlled Fusion* **40** 1767–1773
[34] Dux R, Peeters A G, Kallenbach A, Neu R and Team A U 1999 in *Proceedings of the 26th ESP Conference* European Physical Society, Petit-Lancy volume 23J 1409
[35] Kagan G 2009 Finite Drift Orbit Effects in a Tokamak Pedestal Ph.D. thesis Massachusetts Institute of Technology
[36] Trubnikov R A 1965 *Review Plasma Physics* **1** 105
[37] Groebner R J and Carlstrom T N 1998 *Plasma Physics and Controlled Fusion* **40** 673
[38] Groebner R J, Carlstrom T N and Burrell K H 1996 Study of H-mode threshold conditions in DIII-D Technical Report GA-A22443 General Atomics